Chapter 3

Experimental Procedures

3.1   General settings of the experiment

All rare-earth films and layered structures were prepared *in-situ* by metal-vapor deposition in ultra-high vacuum ($2 - 4 \times 10^{-10}$ mbar during evaporation) on a coin-shaped W(110) single-crystal substrate of 7.5 mm diameter. The substrate was fixed to the sample holder (made of copper) via a sapphire plate (2 mm thick) which provides good thermal conduction at low temperatures but insulates thermally at high temperatures. This allows one to reach temperatures in a range from $\sim$ 20 K to $\sim$ 2000 K [1]. The Gd films were magnetized by an externally applied magnetic field (500 Oe) along the substrate bcc[110] axis which is parallel to the magnetic easy-in-plane axis of epitaxially grown Gd films (hcp b-axis). Tb metal films were magnetized along the same axis by *Curie-point writing*[2]. Magnetic fields were applied using a rotatable electromagnet with a soft-iron yoke that had been especially designed for the present experiments (cf. section 3.4).

The temperature was measured with a W-Re thermo-couple (connected directly to the tungsten crystal) with reference to 0 °C (ice water). The thermo-couple wires were lead into the UHV chamber by means of a glued feed-through in order to avoid undefined contact voltages (appeared in former attempts using a commercial c-type thermo-couple feed-through). For measurements at constant temperature a computer-controlled feed-back regulator was used, with an accuracy of ± 1 K near room temperature and ± 3 K at low temperatures (50 K).

A schematic draft of the arrangement for MOKE measurements in the visible-light region as well as in the x-ray region is depicted in Fig. 3.1. The sample holder in the center of the chamber and the *in-situ* Si-diode at the periphery of the chamber (both rotatable) are vertical-coaxially aligned. Fig. 3.1(a) shows a schematic (top) view of the experimental chamber as circularly polarized light is taken from a synchrotron-radiation beam-line. The sample together with the Si-diode can be adjusted in $\theta - 2\theta$ geometry. Fig. 3.1(b) shows the experiment with visible light provided by a laser. The light is introduced from outside

---

[1] High temperatures up to 2200 K are required to clean the tungsten crystal.
[2] Applying a magnetic field in the paramagnetic phase and then cooling down.
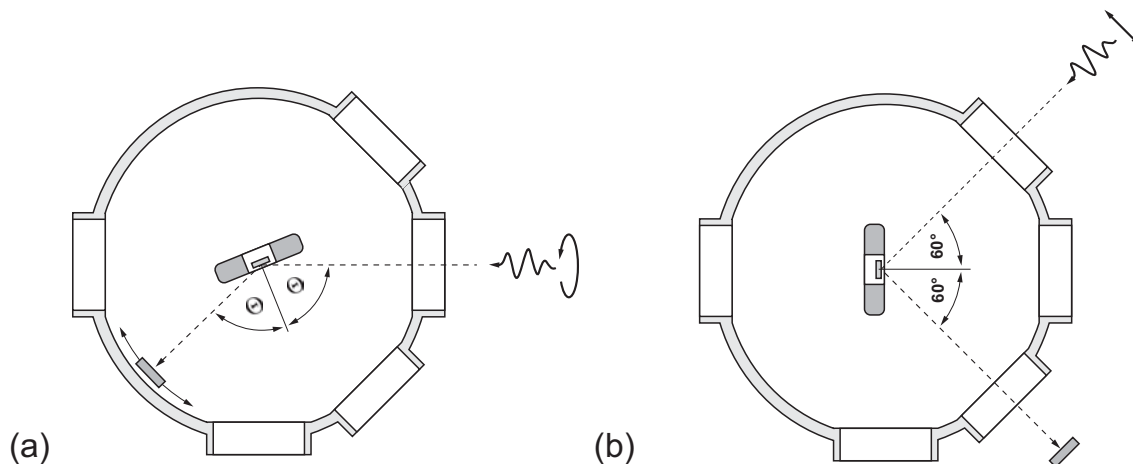
Figure 3.1. (a) In XMOKE experiments the reflected x-ray intensity is collected by an *in-situ* rotatable Si photodiode. Diode and sample are adjustable in $\theta - 2\theta$ geometry. (b) For visible-light MOKE experiments the light beam is supplied by a 10-mW HeNe laser ($\lambda = 633$ nm). The incident and reflected light beams, respectively, enter and exit the chamber through window flanges at $(60 \pm 2)°$ w.r.t. the normal to the sample surface.

the vacuum chamber and the angle of incidence is restricted by the position of the window flanges (here 60° with respect to normal incidence).
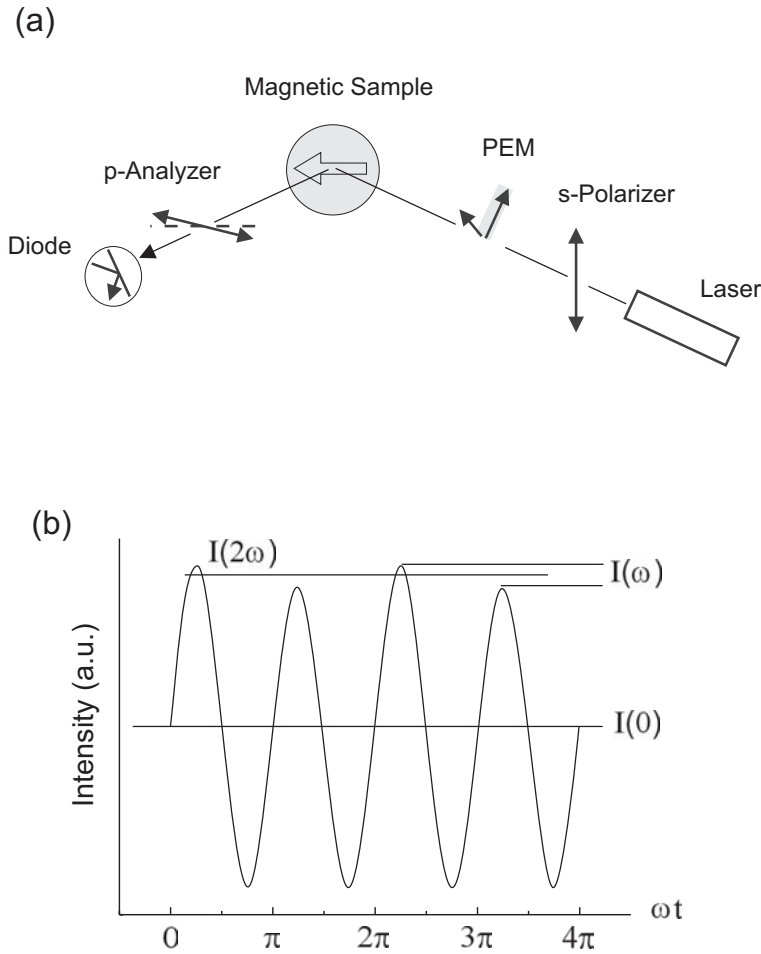
3.2   Set-up for visible-light MOKE measurements

In this subsection we describe the experimental setup which we have used for visible-light MOKE measurements. In addition we give formulae for the MO signal that is measured using a *lock-in modulation* technique, considering the specific experimental geometry of the present setup.

The term MOKE (magneto-optical Kerr effect) represents the phenomenon of linearly polarized light that is reflected from a ferromagnetic sample surface with a slightly rotated plane of polarization (and some ellipticity); this generally complex Kerr rotation is approximately proportional to the sample magnetization. In order to understand the optical setup used in the present work it is useful to remember that many aspects of the propagation of coherent Laser light, including reflection at surfaces of absorbing media, can be well described as superposition of s- and p-polarized plane monochromatic waves.[3] Inside the material the propagating light wave amplitude is damped and shifted in phase according to [43]

$$\vec{E}(r,t)_{medium} = \vec{E}(r,t)_{vacuum} \cdot \underbrace{e^{-i(2\pi\delta/\lambda)z}}_{phase\ shift} \cdot \underbrace{e^{-(2\pi\beta/\lambda)z}}_{damping} . \tag{3.1}$$

---

[3]s-polarized: E-vector is perpendicular (German: *'senkrecht'*) to the light scattering plane; p-polarized: E-vector is *parallel* to the light scattering plane.

(a)

(b)

Figure 3.2. (a) Setup for visible-light MOKE experiments using a lock-in modulation technique. (b) The modulated reflected light intensity as measured by a photodiode. The $I(\omega)$ contribution vanishes when analyzer and polarizer are fully 'crossed'.

δ and β are the usual optical constants ($n = 1 - \delta + i\beta$), z is the distance from the sample surface, and λ is the wavelength. The Kerr amplitude, generated at a depth z, propagates back to the surface being absorbed and shifted in phase on its way back. Thus the information depth of the Kerr effect is roughly *half the light-penetration depth* $l_{abs} = \lambda/(4\pi\beta)$ [93]. In the visible light region the light-penetration depth is on the order of 20 nm for metals.

Kerr rotations in the visible-light region are typically on the order of 10^{-3} rad for ferromagnetic metals [94]. A proper detection of the Kerr signal thus requires either beam-splitting [95] or some lock-in modulation technique [96]; based on earlier experience [97] we opted for the latter. The experimental set-up is schematically shown in Fig. 3.2(a). As light source we used a 633-nm diode laser (10 mW power) with a polarizer set for s-polarized light. The incident beam is modulated (at 50 kHz) with a photo-elastic modulator (PEM); this unit must be rotated about the beam axis by 45° with respect to the incident light polarization [98]. Mostly the p-component of the *reflected beam* is selected with an analyzer that is set so that it mainly accepts p-polarized light (nearly but not exactly 'crossed'). The total intensity is measured using a commercial Si photodiode [99].

Following common practice we employ the Jones matrix formalism in which the reflection from a surface is described by a 2×2 matrix

$$R = \begin{pmatrix} r_p & k \\ -k & r_s \end{pmatrix} , \tag{3.2}$$

with the (complex) diagonal components r_p and r_s giving the reflected amplitudes and phases in the case of a non-magnetic sample. The off-diagonal Kerr components $\pm k$ mix s- and p-components owing the magneto-optical activity of the sample. (k is odd with respect to magnetization reversal.) This means that the incoming p-polarized light generates an s-polarized component and vice versa. In our case the magnetization lies parallel to the sample surface and in the plane of incidence, corresponding to the so-called *longitudinal* Kerr geometry.

The reflected light intensity can be expanded in terms of the modulation frequency and its higher harmonics $I = I(0) + I(\omega) + I(2\omega) + ..$ where $I(0)$ is the dc-contribution, $I(\omega)$ yields the Kerr rotation, and $I(2\omega)$ contains the ellipticity (cf. eq. 3.5). (Higher-order contributions $3\omega, 4\omega, ..$ are small and can be neglected.) For the set-up shown in Fig. 3.2(a) one obtains

$$I(0) = \frac{1}{2} \left\{ r_p^2 (1 - J_0) - 2 \cos \alpha \left[r_p k \cos \delta_{kp} (1 - J_0) + r_s k \cos \delta_{ks} (1 + J_0) \right] \right\} \tag{3.3}$$

$$I(\omega) = 2 J_1 \sin \omega t \left\{ r_p k \sin \delta_{kp} + r_p r_s \sin \Delta \cos \alpha \right\} \tag{3.4}$$

$$I(2\omega) = 2 J_2 \cos 2\omega t \left\{ \frac{1}{2} r_p^2 - (r_s \cos \delta_{ks} + r_p \cos \delta_{kp}) k \cos \alpha \right\} . \tag{3.5}$$

J_0, J_1, and J_2 are the cylindrical Bessel-functions[4], δ_{kp} (δ_{ks}) is the phase between Kerr amplitude and $p-$ ($s-$)light amplitude, and α denotes the angle between polarizer and analyzer defined within $[0, \pi/2]$. A typical example of the modulated reflected intensity as it can be seen with, e.g., an oscilloscope, is shown in Fig. 3.2(b).

Eq. (3.4) reflects two important aspects of the present lock-in detection scheme. The *intensity* at the modulation frequency, $I(\omega)$, is linear in the *Kerr amplitude* and, hence, the difference $I(\omega)^+ - I(\omega)^-$ is proportional to the sample magnetization. The corresponding amplitude $I^+ - I^-$ of this difference signal is (cf. eq. 3.4)

$$I^+ - I^- = 4 J_1 r_p k \sin \delta_{kp} . \tag{3.6}$$

In the sum $I(\omega)^+ + I(\omega)^-$ all contributions proportional to the Kerr amplitude k (odd symmetry w.r.t. magnetization reversal) cancel out; according to eq. 3.4 the amplitude is

$$I^+ + I^- = 4 J_1 r_p r_s \sin \Delta \cos \alpha . \tag{3.7}$$

These linear combinations in eqs. (3.6) and (3.7) will be utilized below to analyze the MOKE signal obtained in temperature dependent magnetization measurements of Gd and Tb films (see Chapter 4).

---

[4] The values of J_0, J_1, and J_2 depend on the modulation amplitude set by the PEM; see, e.g., Ref. [sta91].

3.3 X-ray absorption and reflection

X-ray absorption and reflection experiments were performed at the high-resolution UE56 undulator beamline for elliptically polarized radiation [100] of the Berliner Elektronenspeicherring für Synchrotronstrahlung (BESSY II). The photon energy resolution was set to about 100 meV (FWHM), which is well below the intrinsic width of the narrow Gd $N_{4,5}$ pre-edge absorption lines [101]. The photon energy interval from 110 to 200 eV was scanned at slow speed by a synchronized movement of monochromator and undulator. This synchronization is essential to properly normalize the absorption spectra and allows one to exploit the high flux of the undulator beamline of about 10^{14} photons/(s $\cdot$ 100 mA $\cdot$ 0.1% bandwidth) over a wide energy range. The degree of circular polarization at this Sasaki-type undulator beamline is practically 100 % [100].

The absorption spectra were recorded in total-electron yield (TEY) mode using a high-current channeltron. To suppress the background of secondary electrons from the chamber walls both the sample and a retarding grid placed in front of the channeltron were put on a positiv off-set potential by means of a low-voltage battery. For signal stability high voltage was supplied to the channeltron cathode by using a 3.2 kV battery box. The electron-yield current was amplified by an electrometer set to 3 ms integration time for a scan speed of typically 0.1 eV per second.

If not mentioned otherwise, a light incidence angle of 30° with respect to the film plane was used in order to compromise between a large projection of the CP light wave-vector onto the in-plane film magnetization and the desired sample reflectivity [102]. For XMOKE hysteresis measurements, the x-ray beam diameter was reduced to 0.5 mm by closing the exit slit of the beamline [100]. The specularly reflected x-ray intensity was detected using a commercial Si photodiode which can be rotated on a circle around the sample with an accuracy of some 0.5° inside the UHV chamber. For comparison, visible light MOKE was measured *in-situ* in a similar geometry using a standard laser diode ($\lambda = 635$ nm) and a photoelastic modulator for lock-in detection [97]. Both arrangements are shown in Fig. 3.1.

3.4 Two-axis rotatable magnet

Fig. 3.3 (left panel) gives a schematic picture of the set-up. The electromagnet is mounted at one end of a rotatable axle, and a pair of Helmholtz-like coils (ratio of coil diameter to separation is 1:1) at the other end. The axle itself is held by a fork which can be rotated about ϕ (orthogonal to θ, cf. Fig. 3.3) via a standard rotational feed-through (CF-35). All mechanical parts are made of copper in order to make sure that they cannot be magnetized. To avoid frictional difficulties, that could lead to cold welding of the different parts all bearings are covered by TEFLON$^{\copyright}$. A separate vacuum feed-through is used for the electrical connections. The dimensions of the prototype set-up [37] used in this work are the following: 9 cm diameter of the yoke and 14 cm distance between rotational centre of the set-up and sample position (see Fig. 3.3). The dimensions were chosen in a way

that the distance between coils and yoke are maximum (for the present cylindrical UHV chamber with 30 cm inner diameter) and insertion of the whole set-up into the chamber can be accomplished through a CF-100 flange.
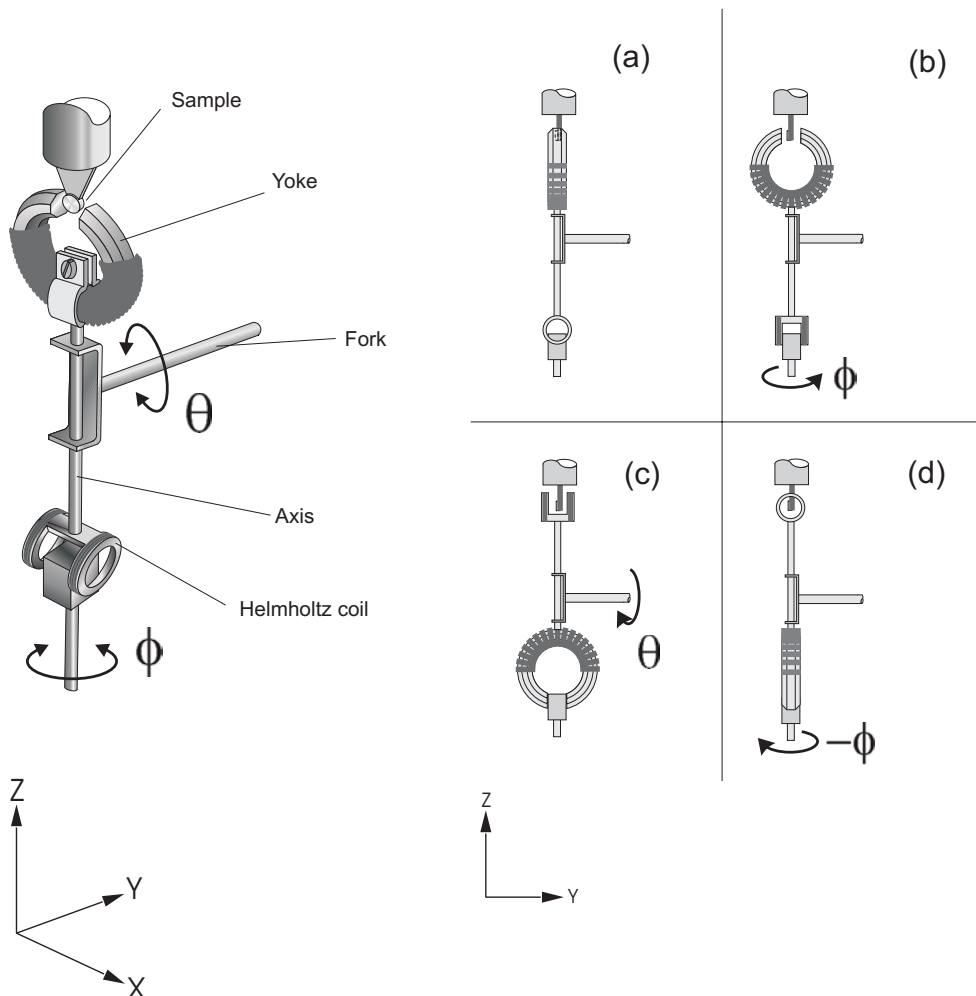
Figure 3.3. (Left panel) Set-up together with the sample in an overview. (Right panel) Exchange sequence of magnet and coils in four steps (for details see text).

The idea of this set-up is to choose either the electromagnet or the coils as a source of external magnetic field, according to the required range of field strengths. The steps to be followed when exchanging electromagnet and coil (or vice versa) are schematically shown on the right panel of Fig. 3.3. In (a) the yoke is in measurement position, with the sample inside the gap. By simultaneous rotation of magnet and sample all orientations in the plane of incidence are accessible, e.g. for $\theta/2\theta$ scans in x-ray scattering experiments. By simple rotation of the magnet, the direction of the external field is adjusted with respect to the sample surface; this permits one e.g. to switch from longitudinal to polar MOKE configuration [8, 103].

To exchange yoke and Helmholtz coil, while leaving the *sample position unchanged*, the
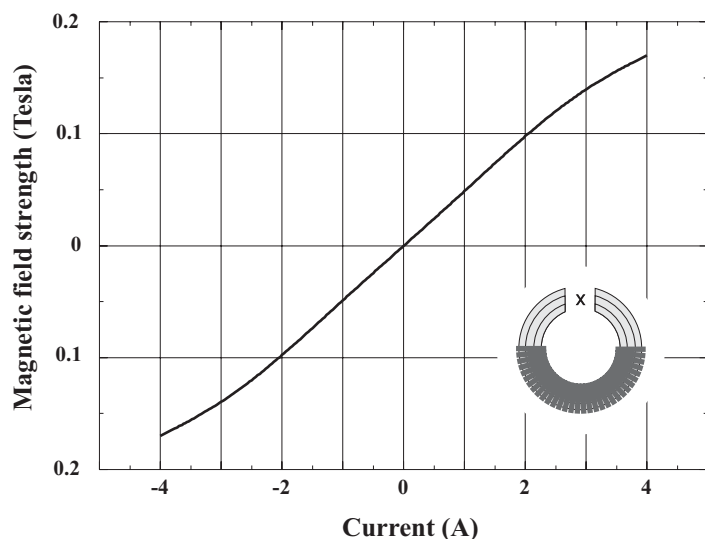
Figure 3.4. Calibration curve of the yoke for mid-gap position, indicated (x) in the inset.

magnet has to be turned around the $z-$axis by a rotational bolt located at the bottom of the chamber until its gap is parallel to the $x-$axis (b). Now the whole set-up can be rotated around ϕ (c) and afterwards turned back into measurement position as shown in (d).

The yoke of the electromagnet is designed in the classical horseshoe shape. We have chosen this shape in order to obtain a strong and highly homogeneous field at the sample position inside the gap (14 mm wide) and to minimize stray fields. The yoke is surrounded by 900 windings of insulated Cu wire, with 0.5 mm diameter. To reduce residual impurities (typically C, S, N) which make iron magnetically hard [8,75] the yoke was annealed for 36 hours in hydrogen atmosphere at 850 °C and afterwards cooled slowly at a rate of $< 30°/$h. By this procedure [104] we reduced the remanence below the earth field and gained a factor of two in maximum field strength in the centre of the gap (1.7 kOe at a current of 4 A). The calibration curve of the yoke is shown in Fig. 3.4, with the non-linear behavior at high fields above 1 kOe likely being a saturation effect of the soft-iron yoke.

In summary, the present prototype two-axis rotatable magnet [37] enables one to exchange yoke and coils in a very easy way which *does not require any movement of the sample.*

3.5 Rare-earth evaporator

In recent years considerable attention has been paid on thin-film and ultrathin-film magnetism of lanthanide metals, and the need for various kinds of ultrahigh vacuum evaporators arose, along with increasing efforts in this field of research. The evaporator used in the present work is a simple home-made electron-beam evaporator shown in a schematic diagram in Fig. 3.5.

The source material (Gd, Tb in the present case) is contained in a tungsten crucible fabricated from a solid rod by spark erosion. The crucible is mounted via a tantalum wire (1 mm diam.) to an electrically insulated feedthrough on a standard CF35 flange.
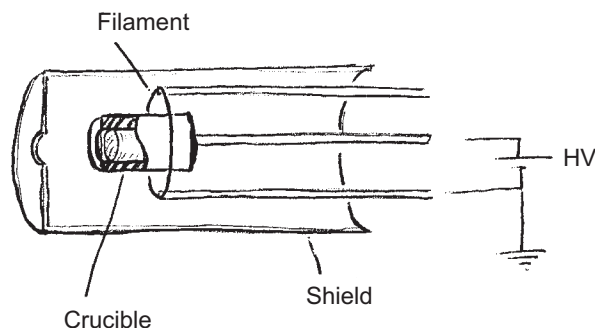
Figure 3.5. Sketch of an electron beam evaporator for lanthanides.

Evaporation is done by electron-beam heating of the crucible at a current of $\sim 2A$, using a 0.125 mm thick tungsten (1% Th) wire surrounding the crucible, with an acceleration potential of 500-800 Volts between filament and crucible. The evaporation cell is shielded by a 0.5 mm thick tantalum foil in order to focus the beam through a 5-mm hole. At a heating power of approximately 45 W a typical deposition rate of $\sim 5\overset{\circ}{A}/\text{min}$ is obtained.

In order to calibrate the evaporator the current between crucible and sample was measured at constant power and constant voltage, regulating the heating power only by the filament current, i.e. the emission of electrons. Under the reasonable assumption that the fraction of ionized atoms in the mass flux is constant at constant high voltage, the deposited charge on the sample was taken as a measure for the film thickness. However, it turned out that calibration is not an easy task. Rigorous grounding was required to avoid charging effects. Regulating the filament current which determines the temperature is extremely difficult. Small variations in the current lead to big changes in emission which destabilizes the regulating behavior. This is perfectly understandable when we look at the equation of Richardson-Dushman which describes the emission rate i_s of electrons from a metal surface at temperature T:

$$i_s \propto T^2 \exp\left(-e\phi/kT\right), \tag{3.8}$$

where ϕ denotes the work function of the surface [105]. The electron emission is extremely sensitive to variations in temperature because of the squared dependence.

The calibration curves shown in Fig. 3.6 are measured with the help of a computer program developed especially for this task which maintains the heating power at a constant level (emission current $\times$ voltage) by regulating the filament current. The characteristics of the evaporator seemed to depend on the source material. In the case of Gd *two different regimes* of operation were detected, depending on the applied voltage and filament current. For a given high voltage (above a given threshold) the emission experiences a sudden strong increase, and the same heating power could be maintained with a filament current reduced by a factor of two. At this considerably smaller filament current it was possible to operate the evaporator with less ohmic heating of the surroundings. This was rewarded by a better
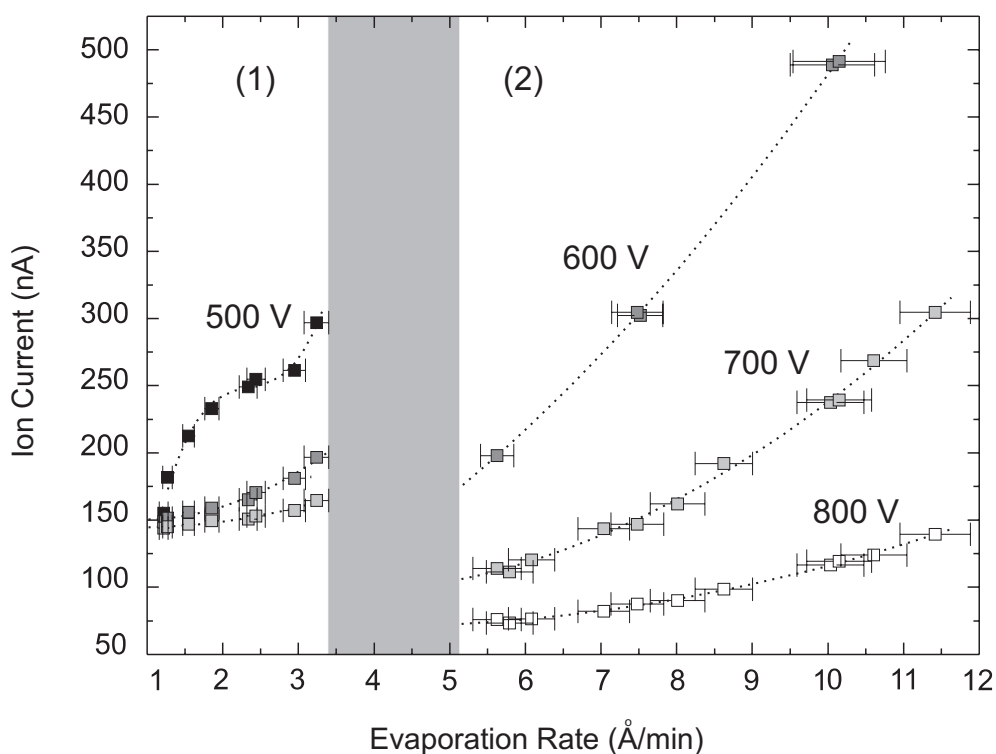
Figure 3.6. Current between crucible and sample at different voltages in the 'normal' region (1) and in the 'amplified' region (2) (the dotted curves serve as guides to the eye).

vacuum chamber pressure that decreased by a factor of five during evaporation.

Reducing the power below the threshold the emission decreases again, and the system drops back into the previous "state". The so-called two states are shown in Fig. 3.6 where (1) is the region of low emission and (2) the region of high emission. Each point of the plot corresponds to a certain power, relating the evaporation rate to the ionic current for a given high voltage. This two-state behavior was not observed for terbium metal.